

HQG-Net: Unpaired Medical Image Enhancement with High-Quality Guidance

Chunming He, Kai Li, *Member, IEEE*, Guoxia Xu, *Member, IEEE*, Jiangpeng Yan, Longxiang Tang, Yulun Zhang, *Member, IEEE*, Xiu Li, *Member, IEEE*, and Yaowei Wang, *Member, IEEE*

Abstract—Unpaired Medical Image Enhancement (UMIE) aims to transform a low-quality (LQ) medical image into a high-quality (HQ) one without relying on paired images for training. While most existing approaches are based on Pix2Pix/CycleGAN and are effective to some extent, they fail to explicitly use HQ information to guide the enhancement process, which can lead to undesired artifacts and structural distortions. In this paper, we propose a novel UMIE approach that avoids the above limitation of existing methods by directly encoding HQ cues into the LQ enhancement process in a variational fashion and thus model the UMIE task under the joint distribution between the LQ and HQ domains. Specifically, we extract features from an HQ image and explicitly insert the features, which are expected to encode HQ cues, into the enhancement network to guide the LQ enhancement with the variational normalization module. We train the enhancement network adversarially with a discriminator to ensure the generated HQ image falls into the HQ domain. We further propose a content-aware loss to guide the enhancement process with wavelet-based pixel-level and multi-encoder-based feature-level constraints. Additionally, as a key motivation for performing image enhancement is to make the enhanced images serve better for downstream tasks, we propose a bi-level learning scheme to optimize the UMIE task and downstream tasks cooperatively, helping generate HQ images both visually appealing and favorable for downstream tasks. Experiments on three medical datasets, including two newly collected datasets, verify that the proposed method outperforms existing techniques in terms of both enhancement quality and downstream task performance. We will make the code and the newly collected datasets publicly available for community study.

Index Terms—Unpaired Medical Image Enhancement, Generative Adversarial Network, Content-Aware Loss, Bi-Level Optimization.

I. INTRODUCTION

Due to the variability of light transmission and clinical imaging conditions, medical images often exhibit uneven illumination or blurry texture details [1]–[3] (see Fig. 1 B and C). These low-quality (LQ) images can significantly impede automated disease screening, examination, and diagnosis. Medical image enhancement aims to transform an LQ image

This work was supported by NSFC 41876098 and Shenzhen Science and Technology Project. (Grant No. JCYJ20200109143041798, WZC20200820200655001). (Corresponding author: Xiu Li) (E-mail: li.xiu@sz.tsinghua.edu.cn)

Chunming He, Jiangpeng Yan, Longxiang Tang, and Xiu Li are with Tsinghua Shenzhen International Graduate School, Tsinghua University, Shenzhen 518055, China. Kai Li is with Machine Learning Department, NEC Laboratories America Inc., NJ 08540, America. Guoxia Xu is with Department of Computer Science, Norwegian University of Science and Technology, 2815 Gjøvik, Norway. Yulun Zhang is with the Computer Vision Lab, ETH Zürich, Zürich 8092, Switzerland. Yaowei Wang is with Peng Cheng Laboratory, Shenzhen 518066, China.

	CCM	Fundus	Colonoscopy
High Contrast	✓		✓
Uniform Illumination		✓	✓
Good Visual Fidelity	✓	✓	✓
Enhanced Texture Details	✓	✓	

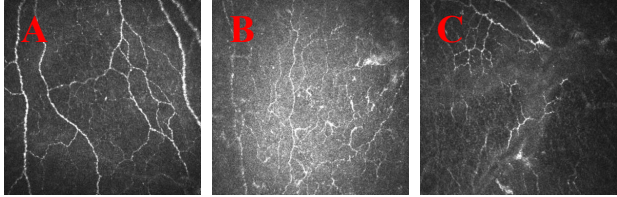


Figure 1: HQ definitions on different medical data [1], [4], [5]. For instance, in Corneal Confocal Microscopy (CCM) data, image A is considered HQ, while B and C are the LQ images. B suffers from low contrast and C has blurred texture details. Despite the degeneracy, all three images still exhibit intra-modality homogeneity.

to a high-quality (HQ) one that fulfills the modality-specific HQ definitions (in Fig. 1), such as enhanced illumination quality and texture details [6]–[8]. Early approaches optimize energy-based objective functions based on certain imaging priors, such as Retinex equation [9], [10] and region line prior [11]. However, these methods are limited in their ability to generalize to different types of degradation conditions, as one imaging prior may only apply to certain types of degradation conditions, restricting their applicability. Recently, deep learning-based methods provide new avenues to this problem and use neural networks to approximate various degradation models. A naive approach involves training a neural network, such as Pix2Pix [12], to translate an LQ image from the LQ domain to the HQ domain at the pixel level. However, this approach requires paired LQ-HQ images with pixel-to-pixel correspondence for training, which can be challenging to obtain for medical applications [1], [13]–[15].

To address the enhancement task more practically, several methods have investigated the unpaired medical image enhancement (UMIE) problem, which requires only unpaired HQ and LQ images as training data. The most intuitive idea is to retain the main structure of Pix2Pix [12] but use specific loss functions for inter-domain structure preservation, e.g., structure loss (Fig. 2 (a)). For instance, EnlightenGAN [16] employs a structure-preserving loss with a global-local discriminator. However, the generator of the Pix2Pix-based method is mainly trained with an unsupervised loss between real LQ and generated HQ images, which neglects valuable

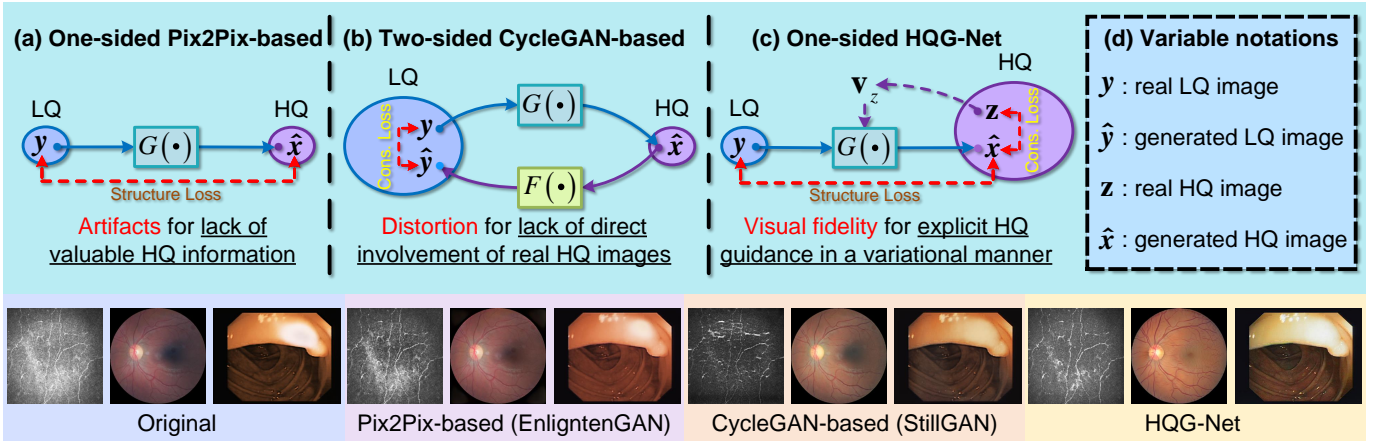


Figure 2: Comparison of different categories of UMIE methods. (a) Pix2Pix-based methods learn a one-sided mapping from the LQ domain to the HQ domain guided by some structure losses. These methods fail to exploit the valuable information from unpaired HQ images. (b) CycleGAN-based approaches are proposed to learn a bi-directional pixel-level map between LQ and HQ domains. (c) the proposed HOG-Net introduces the explicit HQ guidance by injecting the feature vector v_z of an unpaired HQ sample z into the enhancement generator $G(\cdot)$ with two task-specific loss functions.

real HQ information during the training phase, leading to the generation of artifacts in the enhanced medical images. Another approach is to exploit CycleGAN [17], which involves a two-sided translation between LQ and HQ domains for the intra-domain distribution similarity with a cycle-consistent constraint (Fig. 2 (b)). By employing both HQ and LQ images for network training, CycleGAN-based techniques outperform Pix2Pix-based methods in exploiting valuable information from unpaired real HQ images. However, since the real HQ images are not directly involved in the enhancement of LQ images, there exists a domain shift between the enhanced LQ (generated HQ) and the real HQ domains, leading to potential influences on structure fidelity and texture distortion. For structure preservation, StillGAN [1], a CycleGAN-based approach, proposes an SSIM-based structure loss. However, this loss function is applied to the entire image space and can hardly distinguish the complete structure information of LQ medical images with complex degradation.

Considering the intra-modality homogeneity of medical images (Fig. 1), it is desirable to enhance LQ images with the guidance of unpaired but homogeneous HQ images. Therefore, we propose HQG-Net, a GAN-based UMIE network that explicitly utilizes unpaired HQ images as guidance for LQ image enhancement (see Fig. 2 (c)). To ensure the stability of HQG-Net, we introduce the feature vector v_z of an unpaired HQ sample z as guidance. This feature vector is a condensed extraction of HQ information and can moderate the slight degradation from the HQ sample. To preserve structure information from the LQ input, we propose a Variational Information Normalization (VIN) module (see Fig. 3 (c)) that guides the enhancement in a variational manner, where the concise and general variational information ensures the structure preservation of the original image during the domain translation. By introducing the variational guidance information, HQG-Net models the UMIE task under a joint distribution between the LQ and HQ domains, which is supposed to learn more comprehensive and unbiased information [18], [19] and thereby ensures visual fidelity [20].

Furthermore, we propose a content-aware loss to enhance texture details and improve visual fidelity for automated disease screening and diagnosis, incorporating both pixel-level and feature-level constraints. Specifically, the wavelet-based pixel-level constraint ensures inter-domain structure preservation in the high-frequency component, which contains the most abundant texture information, rather than in the whole image space, encouraging the network to focus on translating critical structures from the LQ source image. To address the limited information representation of the pixel-level cycle-consistent loss, we propose a multi-encoder-based feature-level regularization is proposed for intra-domain distribution similarity with deep feature consistency. Due to the domain gap between low-level and high-level vision tasks, a high-quality reconstruction result may not necessarily guarantee good performance on downstream tasks [21], [22] (see Fig. 9). To alleviate this, we propose a cooperative training strategy with a bi-level learning scheme that jointly learns the UMIE task and the downstream tasks such as medical image segmentation and medical image classification. The aim is to generate HQ enhanced results that are both visually appealing and favorable for the downstream tasks.

To comprehensively evaluate the proposed method, we collect two datasets (named *Fundus* and *Colonoscopy* datasets) in addition to the one currently used in this field [1]. Our experiments on the three datasets comprehensively show that HQG-Net consistently outperforms the existing methods.

Our contributions are summarized in the following respects:

- We propose HQG-Net, which incorporates HQ cues to guide LQ image enhancement. In this way, we model UMIE under the joint distribution between LQ and HQ domains that contains more complete and unbiased information, and thus ensures the stability of the framework and improves the visual fidelity of the enhanced result.
- We introduce a content-aware loss for textural enhancement and visual fidelity with the wavelet-based pixel-level and the multi-encoder-based feature-level constraints.
- We propose a plug-and-play cooperative training strategy

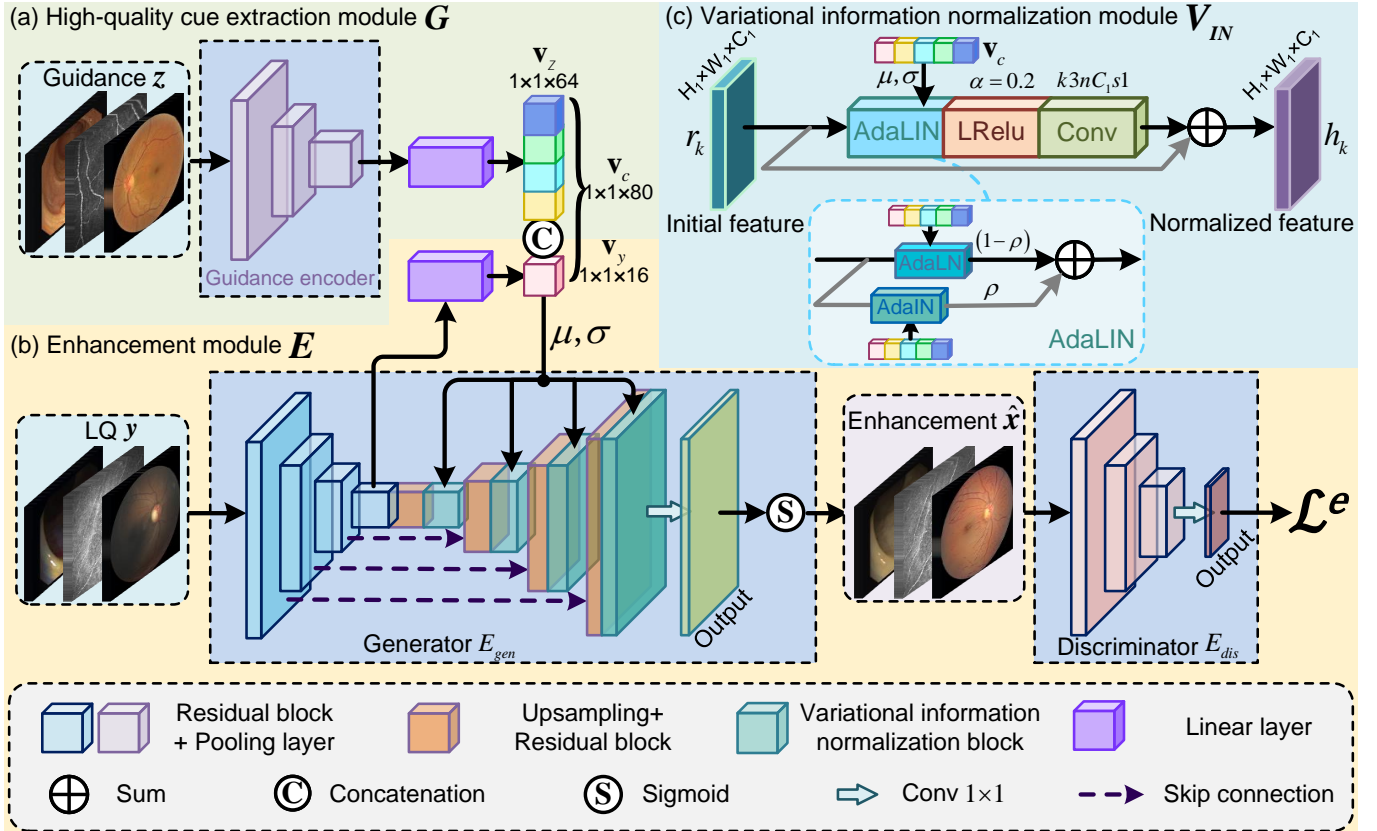


Figure 3: Framework of the proposed HQG-Net. “LRelu” and “Conv” are short for LeakyReLU and convolution, where k, n, s in $k3nC_1s1$ denote kernel, channel, stride. For clarity, we omit other inputs to the discriminator. Following [23] and [1], the backbone of the high-quality cue extraction module G and the generator of the enhancement module E_{gen} are ResNet-18 and ResUNet50. The encoder and decoder of E_{gen} are denoted as E_e and E_d , where E_d has several extra variational information normalization (VIN) modules to inject HQ cues. In E_{gen} , feature maps f_k, r_k, h_k ($k \in \{1, 2, 3, 4\}$) are generated by the basic encoder (the blue blocks), the basic decoder (the orange blocks), the VIN modules (the dark green blocks), respectively.

with a bi-level optimization formulation to produce a better downstream performance as well as enhanced results with better visually appealing effects.

- We conduct extensive experiments on three datasets, including two newly collected datasets, and the results show that HQG-Net achieves state-of-the-art (SOTA) performance in terms of enhancement quality, downstream task performance, and computational efficiency. The newly collected datasets will be made publicly available.

II. RELATED WORK

A. Medical Image Enhancement

Approaches to medical image enhancement can be broadly categorized into model-based and learning-based methods. Model-based methods involve exploiting a specific manually designed imaging prior and then empirically correcting the LQ image correction. Early techniques focused on the global enhancement of the LQ images through stretching the parameters of dynamic ranges, such as histogram equalization (HE) [24], image contrast normalization (ICN) [25], and contrast limited adaptive histogram equalization (CLAHE) [26]. Retinex-based methods [9], [10] were later proposed by decomposing the LQ image into reflectance and illumination parts and recovering them with the corresponding prior knowledge. Additionally,

IDRLP [11] discovered a region line prior to enhance the LQ images with a region fidelity constraint. However, those traditional methods are primarily based on manually designed imaging priors, which fail to handle the complex degradation conditions and thus suffer from the limited application scope.

Learning-based methods are more flexible and can be extended to the unpaired setting, where paired LQ-HQ images are not required for model training. Intuitively, the unpaired problem can be solved by the structure of Pix2Pix [12] with task-specific loss functions in an unsupervised framework [16], [27]. ADN [27] employed multiple encoders and decoders to separate the content information from the degraded component and train the network with specialized loss in an unsupervised manner. EnlightenGAN [16] proposed a multi-scale discriminator with a structure-preserving loss. Nevertheless, those Pix2Pix-based networks neglect the valuable information from the unpaired HQ images, which weakens their resilience to complex degradation conditions. To exploit the unpaired LQ and HQ images, CycleGAN [17] was proposed with the cycle consistency constraint to learn a mapping between the LQ and the HQ domains. StillGAN [1] was a CycleGAN-based method with a structure preservation loss and an illumination constraint. Unfortunately, the two-sided cycle-consistency strategy lacks the direct involvement of HQ images in the

enhancement of LQ images, which inevitably brings domain shift and thus results in structure distortion [28]. To solve these problems, we propose the explicit guidance-based HQG-Net with the variational information normalization module and the content-aware loss for structure preservation and visual fidelity. Furthermore, we design a plug-and-play cooperative training strategy to simultaneously acquire visual-appealing enhancement results and satisfactory downstream applications.

B. Reference-based Super-Resolution and Style Transfer

Our HQG-Net is also related to reference-based image super-resolution (Ref-SR) and Style Transfer (Ref-ST), which mainly focus on natural images. While it may seem straightforward to extend methods from these fields to medical images, we argue that such naive extension often fails to produce satisfactory results as the unique characteristics of medical images are not properly modeled. In reference-based image super-resolution (Ref-SR), the generation of texture details heavily relies on the reference image via point-wise or patch-wise correspondence. CrossNet [29] established a relationship between the reference image and the low-resolution (LR) image by flow estimation for point-wise alignment. For patch matching, NTT [30] matched the multi-level features extracted from a pretrained VGG between the reference image and LR image in a concatenated manner. Style transfer aims to generate a restylized image by rendering the source image with the style component from a given reference image. By embedding the encoded reference image into a latent space, StyleGAN [31] enabled controlled modifications in style transfer. To generate diverse images across multiple domains, StarGAN V2 [23] introduced a style mapping network with domain-specific style codes extracted by specific reference images.

It should be noted that we are the **first** to handle the UMIE problem with the explicit assistance of reference images. Besides this, HQG-Net differs from existing Ref-SR and Ref-ST methods in several aspects. **First**, unlike source images in ref-SR or ref-ST that are of high quality, LQ images in UMIE often suffer from complex degradation conditions [32], such as light transmission disturbance and environment-induced artifacts. Therefore, a stable HQ cue extractor and general guidance are required to handle the complex degradation. To achieve this, we pretrain the HQ cue extraction module G with images from both LQ and HQ domains to achieve stable HQ cue extraction and guide the enhancement in a condensed variational manner with the purpose of general guidance. **Second**, different from ref-ST and ref-SR, which prioritize visually appealing results, UMIE also emphasizes structure preservation for clinical requirements [1]. However, both the feature-level alignment (ref-SR) and the reference-only guidance manner (ref-ST) can inevitably suppress the structure preservation capacity. To accommodate this requirement, we propose the task-specific content-aware loss and make two additional changes to our HQG-Net, including guiding the enhancement with the joint variational vector \mathbf{v}_c (including \mathbf{v}_z and \mathbf{v}_y), and using the adaptive normalization operator *AdaLIN*. By employing the joint vector and the adaptive normalization operator, we expect the enhanced results to simultaneously ensure high-quality reconstruction performance and preserve the critical

Table I: Summation of the primary notations used in this paper.

Notations	Meanings
Data	
\mathbf{z}	HQ guidance image
\mathbf{y}	LQ image
$\tilde{\mathbf{x}}$	Enhanced result of the LQ image
Guidance vectors	
\mathbf{v}_z	HQ guidance vector
\mathbf{v}_y	LQ structure vector
\mathbf{v}_c	Joint vector
Feature maps	
f_k	Feature maps of the encoder E_e
r_k, h_k	Feature maps of the decoder E_d before and after being processed by the variational information normalization module

structure information with the joint guidance strategy and the learnable hybrid normalization operation.

III. METHODOLOGY

Unpaired Medical Image Enhancement (UMIE) aims to learn an enhancement model with a low-quality (LQ) image dataset \mathcal{Y} and a high-quality (HQ) image dataset \mathcal{Z} . Note that \mathcal{Y} and \mathcal{Z} are unpaired, i.e., there is not an image from \mathcal{Z} that is the high-quality version of an image from \mathcal{Y} . We propose a novel UMIE technique, dubbed HQG-Net, by explicitly employing HQ information to guide the enhancement of the LQ image. For structure preservation and visual fidelity, a novel content-aware loss is designed with the wavelet-based pixel-level constraint and the multi-encoder-based feature-level regularization. Furthermore, we propose a cooperative training strategy with a bi-level optimization formulation to produce a better downstream performance as well as visually appealing enhanced results. For better comprehension, we summarize the primary notations utilized in this paper, along with their corresponding meanings, in Table I.

A. Network Architecture

HQG-Net consists of four main parts, including a high-quality cue extraction module G , a generator E_{gen} of the enhancement module E , a variational information normalization module V_{IN} , and a discriminator E_{dis} , where V_{IN} convey the HQ cue from G to E for high-quality (HQ) guidance. The specific network architecture of HQG-Net is shown in Fig. 3. **High-quality cue extraction.** An HQ image \mathbf{z} is randomly selected and then feed into G to extract high quality cues,

$$\mathbf{v}_z = G(\mathbf{z}), \quad (1)$$

where $\mathbf{z} \in \mathcal{Z}$, $\mathbf{v}_z \in \mathbb{R}^{d_z}$ is the vector with h -dimension expected to encode HQ cue and $h = 64$. Following [23], we implement G as ResNet-18, plus a full-connected (FC) layer to get the guidance vector. To facilitate HQ cue extraction, we pretrain ResNet-18 within an auto-encoder framework. Specifically, we use ResNet-18 as an encoder, append a decoder with the transposed structure, and pretrain the encoder-decoder model with the standard MSE loss and SSIM loss [33]. Apart from the HQ images from \mathcal{Z} , we pretrain the model with additional LQ images from \mathcal{Y} to ensure its robustness to the latent subtle perturbations in the HQ guidance image and thus facilitate the extraction of stable HQ cues.

Guided low-quality image enhancement. Following [1], our enhancement network is based on ResUNet50 with the last layer abandoned for computational efficiency. Besides, we plus several extra Variational Information Normalization (VIN) Modules that inject HQ cues in multiple levels. Specifically, given an LQ image $\mathbf{y} \in \mathcal{Y}$, the ResNet50 encoder E_e generates a set of feature maps f_k ($k \in \{1, 2, 3, 4\}$) in different levels.

Considering that the latent domain discrepancy between the LQ input \mathbf{y} and the HQ guidance \mathbf{z} can affect the quality of image enhancement, it is desirable to generate the enhanced result $\hat{\mathbf{x}}$ with the joint guidance of \mathbf{y} and \mathbf{z} to simultaneously ensure the high-quality reconstruction and preserve the significant semantic information. Therefore, we map f_4 to a compact vector $\mathbf{v}_y \in \mathbb{R}^{16}$, which is expected to contain critical structural information, by a linear layer FC_e , i.e., $\mathbf{v}_y = FC_e(E_e(\mathbf{y}))$. We concatenate \mathbf{v}_y with the extracted HQ vector \mathbf{v}_z and thus obtain the integrated joint vector \mathbf{v}_c

$$\mathbf{v}_c = \text{concat}(\mathbf{v}_z, \mathbf{v}_y), \quad (2)$$

which encodes the gist information from both the LQ image \mathbf{y} and the HQ image \mathbf{z} , and we use \mathbf{v}_c as one input for the VIN modules inserted into the decoder in a multi-scale manner.

The decoder E_d also has a ResNet50-like backbone with four layers, except a VIN module appended after each residual block in the decoder. Each layer of the decoder consists of two components, the residual block and the VIN, which produce the corresponding output feature maps r_k and h_k , $k \in \{1, 2, 3, 4\}$. In the residual block, the spatial resolution of the feature map h_{k+1} is first up-sampled by a factor of 2. Then the up-sampled feature is concatenated with the feature f_k from the encoder and compressed by a 1×1 convolution to reduce channel dimensions. The compressed feature map is further processed by a 3×3 convolution and generates the output feature map of the residual block r_k :

$$r_k = \text{conv3}(\text{conv1}(\text{concat}(\text{up_sample}(h_{k+1}), f_k))), \quad (3)$$

where up_sample , conv1 , conv3 denote up-sampling, 1×1 , and 3×3 operations, respectively. Note that $r_4 = \text{conv3}(f_4)$.

Variational information normalization (VIN). As shown in Fig. 3 (c), the VIN module takes the feature map r_k and the guidance of vector \mathbf{v}_c as inputs, and outputs an HQ-aware feature map h_k that is combined with the decoded feature map r_k for further processing. VIN is a residual connection structure with AdaLIN, LReLU, and a 3×3 convolution layer. Therefore, the final feature map h_k is formulated as follows:

$$\begin{aligned} h_k &= \text{VIN}(r_k, \mathbf{v}_c), \\ &= \text{conv3}(\text{AdaLIN}(r_k, \mathbf{v}_c)), \end{aligned} \quad (4)$$

where AdaLIN is the AdaLIN operator, which is an information normalization block by combining the adaptive instance normalization (AdaIN) [34] and the adaptive layer normalization (AdaLN) [35] with a learnable parameter. The definition of the proposed AdaLIN is presented as follows:

$$\text{AdaLIN} = \rho \text{AdaIN} + (1 - \rho) \text{AdaLN}, \quad (5)$$

where ρ is a learnable parameter and is initialized as 0.5. Although AdaIN and AdaLN focus on instance and layer separately, they share a common structure with the same

mathematical formulation. Take AdaIN as an example:

$$\text{AdaIN}(r_k, \mathbf{v}_c) = \sigma(\mathbf{v}_c) \left(\frac{r_k - \mu(r_k)}{\sigma(r_k)} \right) + \mu(\mathbf{v}_c), \quad (6)$$

where μ and σ correspond to mean and variance value. Being normalized by the concise and general variational information from the joint vector \mathbf{v}_c (including \mathbf{v}_z and \mathbf{v}_y), HQG-Net can simultaneously exploit the HQ cues extracted from the vector-based HQ guidance and preserve significant structural information from the LQ input. This ensures the generation of enhancement results with visual fidelity and structure preservation, thereby facilitating clinical decision-making.

Discriminator. Our discriminator E_{dis} is constructed following PatchGAN [36] with patch-wise strategy, which is particularly beneficial for the LQ medical images with complex degraded conditions [37], e.g., blur and retinal artifact [10], and thus ensures the enhancement performance.

B. Content-Aware Loss

Previous enhancement losses focus on the pixel-level consistency on both paired settings, e.g., mean square error, and unpaired conditions, e.g., cycle-consistency loss [1], for the structure preservation and visual fidelity, which brings two problems for UMIE. First, it can be challenging for pixel-level constraints to distinguish the complete structural information between the concerning biological tissues and LQ factors, especially for complex degradations. Therefore, a preliminary structure extraction operation can benefit the pixel-level loss function. Besides, the pixel-level constraint suffers from limited information, whereas in-depth features have a more robust representation capacity. Hence, an additional feature-level constraint is desirable to supplement this deficiency.

Since structural information is predominantly encoded in high-frequency components [38] while exhibiting the texture sparsity in the whole image space, it is preferable to encourage structure fidelity in separately extracted high-frequency components rather than the whole-frequency image space. The wavelet-based operator is well-suited to this requirement [13], [39]. To this end, we adopt the Haar wavelet to construct a structure preservation loss, termed \mathcal{L}_{Haar} , between the LQ input \mathbf{y} and the enhanced result $\hat{\mathbf{x}}$. \mathcal{L}_{Haar} is defined as follows:

$$\mathcal{L}_{Haar} = \|\hat{\mathbf{x}}^{HF} - \mathbf{y}^{HF}\|_1, \quad (7)$$

where $\hat{\mathbf{x}}^{HF}$ and \mathbf{y}^{HF} are the integrated high-frequency parts of $\hat{\mathbf{x}}$ and \mathbf{y} filtered by the wavelet-based high pass filters, including the vertical, horizontal, and diagonal filters. \mathcal{L}_{Haar} enforce the network to learn how to utilize the extracted HQ cues without sacrificing structure preservation from the LQ input, thus reducing the risk of misleading medical decisions.

For the second problem, a feature consistency loss, dubbed \mathcal{L}_{FC} , is proposed by constraining the feature-level consistency between the enhanced result $\hat{\mathbf{x}}$ and the comprehensive guidance \mathbf{v}_c in a vector form, which is formulated as:

$$\mathcal{L}_{FC} = \|Gr(\mathbf{v}_{\hat{\mathbf{x}}}) - Gr(\mathbf{v}_c)\|_F, \quad (8)$$

where $\mathbf{v}_{\hat{\mathbf{x}}} = \text{concat}(G(\hat{\mathbf{x}}), FC_e(E_e(\hat{\mathbf{x}})))$, $Gr(\cdot)$ represents the Gram matrix [40] for a more abstract feature characterization. $\|\cdot\|_F$ denotes Frobenius norm. As presented in Eq. 8, the enhanced result $\hat{\mathbf{x}}$ is expected to share a similar representation with the generated encoding information of

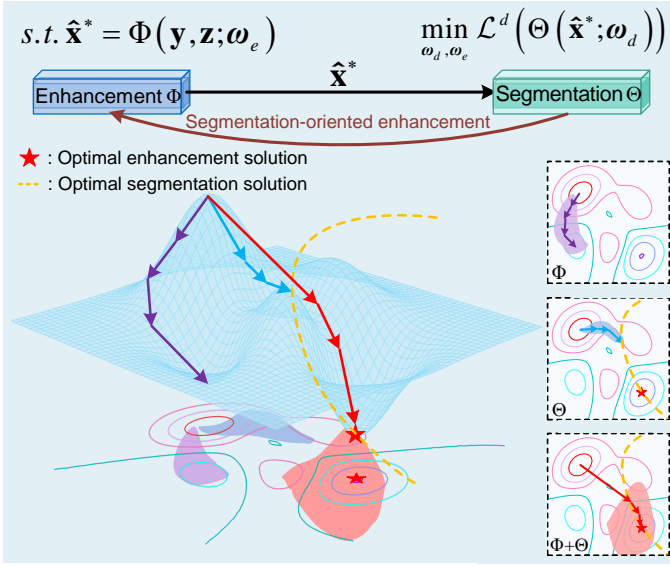


Figure 4: Bi-level optimization formulation and cooperative training strategy, where the right three contour plots denote the optimization processes constrained by the enhancement Φ , the segmentation Θ , and the bi-level strategy $\Phi + \Theta$.

the LQ input and the variational encoding feature of the HQ guidance in a compact vector form. Such a constraint contributes to the extraction of general HQ cues and ensures that the extracted HQ cues can be fully leveraged for image enhancement, thereby jointly ensuring the retention of feature-level information and visual fidelity.

Combining the Haar wavelet-based loss and feature consistency loss, we propose a content-aware loss, \mathcal{L}_{CA} , for structure preservation, textural enhancement, and visual fidelity:

$$\begin{aligned} \mathcal{L}_{CA} &= \mathcal{L}_{Haar} + \lambda_1 \mathcal{L}_{FC}, \\ &= \|\hat{\mathbf{x}}^{HF} - \mathbf{y}^{HF}\|_1 + \lambda_1 \|Gr(\mathbf{v}_{\hat{\mathbf{x}}}) - Gr(\mathbf{v}_c)\|_F, \end{aligned} \quad (9)$$

where λ_1 is a trade-off parameter. Intuitively, the content-aware loss balances the structural preservation from LQ input \mathbf{y} , and the feature-based visual fidelity from HQ guidance \mathbf{z} .

Apart from the content-aware loss, a standard GAN loss is used for the adversarial training to simultaneously regularize the generation ability and discrimination capability:

$$\begin{aligned} \mathcal{L}_{GAN} &= \min_{E_{gen}} \max_{E_{dis}} \mathcal{L}(E_{gen}, E_{dis}), \\ &= \mathbb{E}_{\mathbf{y}} [\log E_{dis}(\mathbf{y})] + \mathbb{E}_{\mathbf{y}, \mathbf{z}} [\log(1 - E_{dis}(\hat{\mathbf{x}}))], \end{aligned} \quad (10)$$

where $E_{gen}(\cdot)$ generates an enhanced result $\hat{\mathbf{x}}$ conditioned on the LQ image \mathbf{y} and the guidance image \mathbf{z} , while $E_{dis}(\cdot)$ tries to distinguish the differences between LQ and HQ images.

Combining the content-aware loss and the standard GAN loss, we reach our enhancement-oriented learning objective as

$$\mathcal{L}^e = \mathcal{L}_{CA} + \lambda_2 \mathcal{L}_{GAN}, \quad (11)$$

where λ_2 is the trade-off parameter.

C. Bi-level Optimization and Cooperative Training

Bi-level optimization. Due to discrepancies in domain knowledge and training strategy, there inevitably exists a significant domain gap between low-level vision problems and subsequent high-level tasks, i.e., a high-quality reconstruction result in the low-level domain may not necessarily result in a good

performance in high-level tasks [41]. Inspired by the success of bi-level optimization (BLO) in parameter optimization that jointly updates the model parameters and the hyper-parameters [42], we introduce BLO to UMIE, aiming to achieve satisfactory performance on both the UMIE problem and downstream tasks. Following the truism Stackelberg's theory [43], the segmentation-oriented enhancement is defined as a BLO formulation, which is formulated as follows:

$$\min_{\omega_d} \mathcal{L}^d(\Theta(\hat{\mathbf{x}}^*; \omega_d)), \quad (12)$$

$$s.t. \hat{\mathbf{x}}^* \in \arg \min_{\hat{\mathbf{x}}} f(\hat{\mathbf{x}}; \mathbf{y}, \mathbf{z}) + g_e(\hat{\mathbf{x}}; \mathbf{y}) + g_v(\hat{\mathbf{x}}; \mathbf{z}), \quad (13)$$

where \mathcal{L}^d is the objective function for the segmentation task and $\Theta(\cdot; \omega_d)$ represents the segmentation network enabled by the trainable parameters ω_d . $f(\cdot)$ is the enhancement term jointly driven by the two feasible constraints $g_e(\cdot)$ and $g_v(\cdot)$.

As presented in Fig. 4, the proposed bi-level formulation can improve the performance of both enhancement and segmentation tasks. Paradoxically, the ill-posed constraint in Eq. 13 is not bound in the form of an equation, which inevitably brings challenges for further optimization. Consequently, it is desirable to replace the complicated constraints with an adaptive framework and unroll the bi-level formulation into two networks, i.e., the segmentation network Θ and the enhancement network Φ , which is defined as follows:

$$\min_{\omega_d, \omega_e} \mathcal{L}^d(\Theta(\hat{\mathbf{x}}^*; \omega_d)), \quad s.t. \hat{\mathbf{x}}^* = \Phi(\mathbf{y}, \mathbf{z}; \omega_e), \quad (14)$$

where $\Phi(\cdot; \omega_e)$ is the proposed HQG-Net with the corresponding parameters ω_e . In practice, considering the discrepancy of medical data and medical applications, different deep frameworks are adopted as the backbone for the downstream network Θ under the specific task. In particular, CS-Net [7] and PNS-Net [6] are correspondingly applied as the segmentation network for *CCM* and *colonoscopy* datasets, and Deepgrading [44] are used as the classification network for nerve fiber tortuosity classification task with *CCM* data.

Cooperative training strategy. In this section, we further propose a cooperative training strategy for the jointly optimal network parameters, i.e., $\omega = (\omega_d, \omega_e)$, with the aforementioned bi-level framework. By incorporating the downstream regularizer \mathcal{L}^d and the enhancement regularizer \mathcal{L}^e , Eq. 14 can be rewritten from the perspective of mutual optimization:

$$\min_{\omega_d, \omega_e} \mathcal{L}^d(\Theta(\hat{\mathbf{x}}^*; \omega_d)) + \lambda_3 \mathcal{L}^e(\Phi(\mathbf{y}, \mathbf{z}; \omega_e)), \quad (15)$$

$$s.t. \hat{\mathbf{x}}^* = \Phi(\mathbf{y}, \mathbf{z}; \omega_e), \quad (16)$$

where λ_3 is a hyperparameter for balance. We further present the gradient propagation flow of the parameters of downstream task ω_d and enhancement network ω_e :

$$\frac{\partial \mathcal{L}}{\partial \omega_d} = \frac{\partial \mathcal{L}^d}{\partial \Theta_d} \frac{\partial \Theta_d}{\partial \omega_d}, \quad (17)$$

$$\frac{\partial \mathcal{L}}{\partial \omega_e} = \frac{\partial \mathcal{L}^d}{\partial \Theta_d} \frac{\partial \Theta_d}{\partial \Phi_e} \frac{\partial \Phi_e}{\partial \omega_e} + \lambda_3 \frac{\partial \mathcal{L}^e}{\partial \Phi_e} \frac{\partial \Phi_e}{\partial \omega_e}, \quad (18)$$

where \mathcal{L} denotes the overall energy function Eq. 15, which is subject to Eq. 16. The loss gradient of ω_e is jointly determined by the loss functions of both enhancement and the downstream task, yielding visually pleasant results with favorable downstream performance. Note that under the cooperative training strategy, the enhancement task is not unilaterally

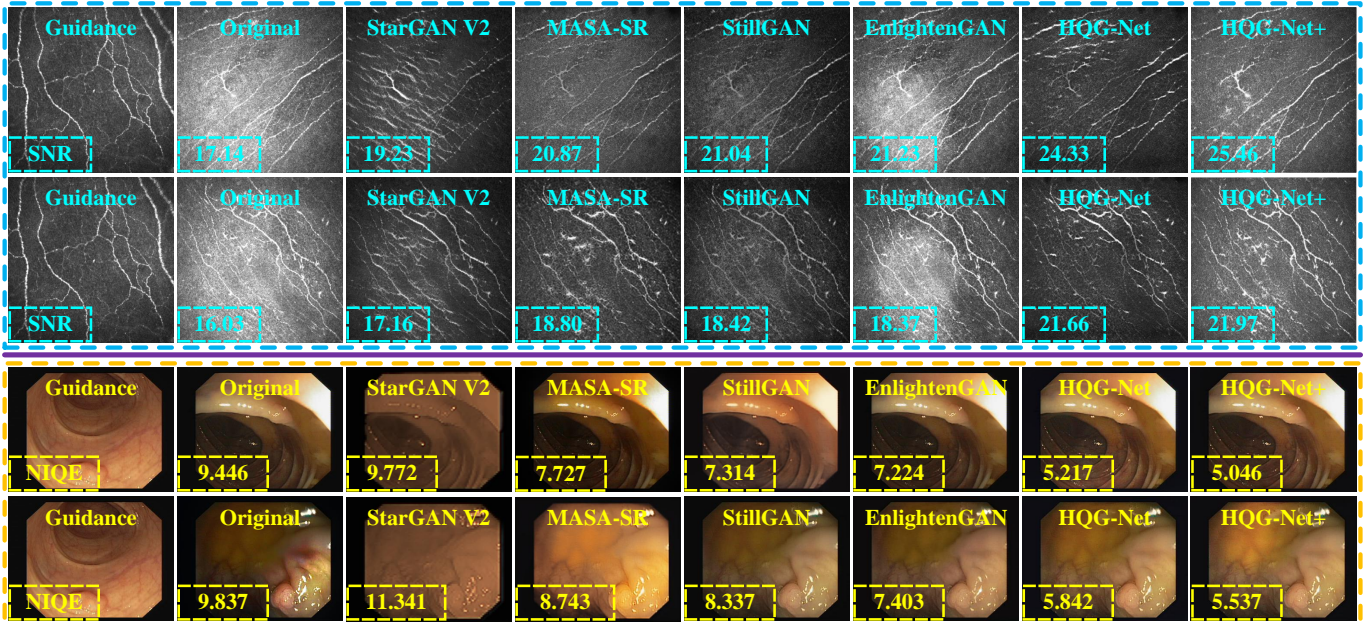


Figure 5: Visual comparison of enhanced results on *CCM* and *Colonoscopy* datasets with guidance images. SNR is $SNR_{r=3}$.

Table II: Details of the used datasets. *CCM* and *Colonoscopy* datasets have the paired segmented labels.

Datasets	Training Set		Test Set		Paired Labels
	HQ	LQ	HQ	LQ	
<i>CCM</i>	288	340	200	60	✓
<i>Colonoscopy</i>	115	270	200	70	✓
<i>Fundus</i>	640	700	200	600	

catered to the downstream task. Conversely, the downstream task can also assist the enhancement task to obtain better enhanced results. For instance, in medical image segmentation, mis-segmentation often occurs at the boundaries that contain crucial structural information and texture details, which are also challenging to highlight for UMIE. In this regard, the enhancement network, with additional constraints on the loss function of the segmentation task, can focus more on the boundary information and thus generate visually pleasant results with preserved structure and enhanced texture. Hence, as shown in Fig. 4, compared to the enhancement network optimized solely with the enhancement loss, the network optimized by our cooperative training strategy with a BLO formulation can achieve a more optimal enhancement solution with the assistance of constraints from the downstream task.

IV. EXPERIMENT

Datasets. We employ three datasets, i.e., the corneal confocal microscopy (*CCM*) dataset, the *Fundus* dataset, and the *Colonoscopy* dataset, to evaluate enhancement performance under complex degeneration conditions. *CCM* dataset is publicly available [1], while *Fundus* and *Colonoscopy* datasets are the private datasets collected and relabelled by our collaborative clinicians into HQ and LQ subsets from the iSee dataset [45] and the CVC-EndoSceneStill dataset [46]. Details of the three datasets are presented in Table II. Note that *CCM* and *Colonoscopy* contain paired segmentation labels for the

HQ and LQ images, which enables us to quantitatively evaluate the enhancement quality by taking segmentation as the downstream task and retrain our framework with the proposed cooperative training strategy for a bi-level optimization.

Implementation details. Our HQG-Net is trained with random flipping for data augmentation. Adam optimizer is applied with momentum terms (0.5, 0.99) and the learning rate is set as 1×10^{-4} . The batch size is set as 4, and the trade-off parameters $\lambda_1, \lambda_2, \lambda_3$ are set as 10, 1, 5, respectively. In the test phase, one HQ image in the corresponding test set is randomly selected as guidance for the LQ input. All the experiments are implemented with PyTorch on two RTX3090TI GPUs.

Compared methods. Ten state-of-the-art (SOTA) methods are selected in comparison, including three traditional methods, i.e., CARFI [9] (Retinex-based), ATA [10] (Retinex-based), and IDRLP [11] (region line prior), and seven learning-based techniques, i.e., StarGAN V2 [23] (style transfer), SSEN [47] (ref-SR), TTSR [48] (ref-SR), C^2 -Matching [49] (ref-SR), MASA-SR [50] (ref-SR), StillGAN [1] (CycleGAN-based), and EnlightenGAN [16] (Pix2Pix-based). Note that we incorporate the style transfer-oriented or ref-SR-based techniques in natural scenarios into our experiment to evaluate the effectiveness of the task-specific modifications of our HQG-Net mentioned in Section II. All the compared methods are trained and tested with their corresponding default settings.

A. Results and Analyses

CCM. All the learning-based methods are trained on the *CCM* dataset [1]. Four metrics, i.e., signal-to-noise ratio (SNR) [1] with a radius of 3, 5, 7, and 9 pixels, are used for quantitative evaluation, where a higher score indicates a better enhancement result. As shown in Table III, the proposed HQG-Net achieves the best performance in all the metrics with a significant improvement. Furthermore, we also provide the results of StarGAN V2+, MASA-SR+, StillGAN+,

Table III: Quantitative evaluation of enhancement quality. The best and second-best results are marked in red and blue, respectively. “+” denotes optimizing the method under the cooperative training strategy. In *CCM* dataset, the cooperative training strategy improves the enhancement result by 6.9% (HQG-Net), 2.5% (EnlightenGAN), 4.9% (StillGAN), 5.3% (MASA-SR), and 1.2% (StarGAN V2). In *Colonoscopy* dataset, the cooperative training strategy increases that by 8.7% (HQG-Net), 5.6% (EnlightenGAN), 3.7% (StillGAN), 2.9% (MASA-SR), and 15.0% (StarGAN V2).

Methods	CCM				Colonoscopy			
	$SNR_{r=3} \uparrow$	$SNR_{r=5} \uparrow$	$SNR_{r=7} \uparrow$	$SNR_{r=9} \uparrow$	AG \uparrow	EN \uparrow	NIQE \downarrow	BRISQUE \downarrow
Original	17.47	17.61	17.65	17.67	1.10	4.29	12.89	51.76
CAEFI [9]	18.12	18.97	19.73	21.35	4.33	6.32	6.82	39.46
ATA [10]	14.27	15.07	17.72	18.83	5.84	6.18	6.43	44.73
IDRLP [11]	15.14	17.54	20.57	21.86	2.59	5.91	6.85	42.07
StarGAN V2 [23]	19.44	19.62	19.76	20.73	3.16	5.97	7.41	41.83
SSEN [47]	19.12	19.52	19.93	21.04	5.96	5.89	9.43	40.45
TTSR [48]	20.78	21.32	22.04	22.93	6.33	6.05	7.57	39.70
C^2 -Matching [49]	20.34	20.85	21.73	21.96	6.07	5.78	7.94	39.86
MASA-SR [50]	21.23	21.78	22.31	22.94	6.50	6.17	7.02	39.05
StillGAN [1]	20.45	21.11	21.94	22.74	6.32	6.56	6.62	39.42
EnlightenGAN [16]	20.22	22.87	23.55	24.37	6.60	6.85	6.69	41.15
HQG-Net	22.68	23.19	25.08	26.14	6.75	7.26	6.61	36.43
StarGAN V2+	19.55	19.78	20.35	20.84	5.26	6.33	7.02	38.83
MASA-SR+	22.37	23.06	23.41	24.10	6.54	6.33	7.01	38.94
StillGAN+	21.74	22.35	22.87	23.42	6.38	6.67	6.54	39.33
EnlightenGAN+	21.03	23.28	23.97	24.93	6.68	6.87	6.68	39.31
HQG-Net+	24.13	26.24	26.87	27.12	6.93	6.92	6.43	33.17

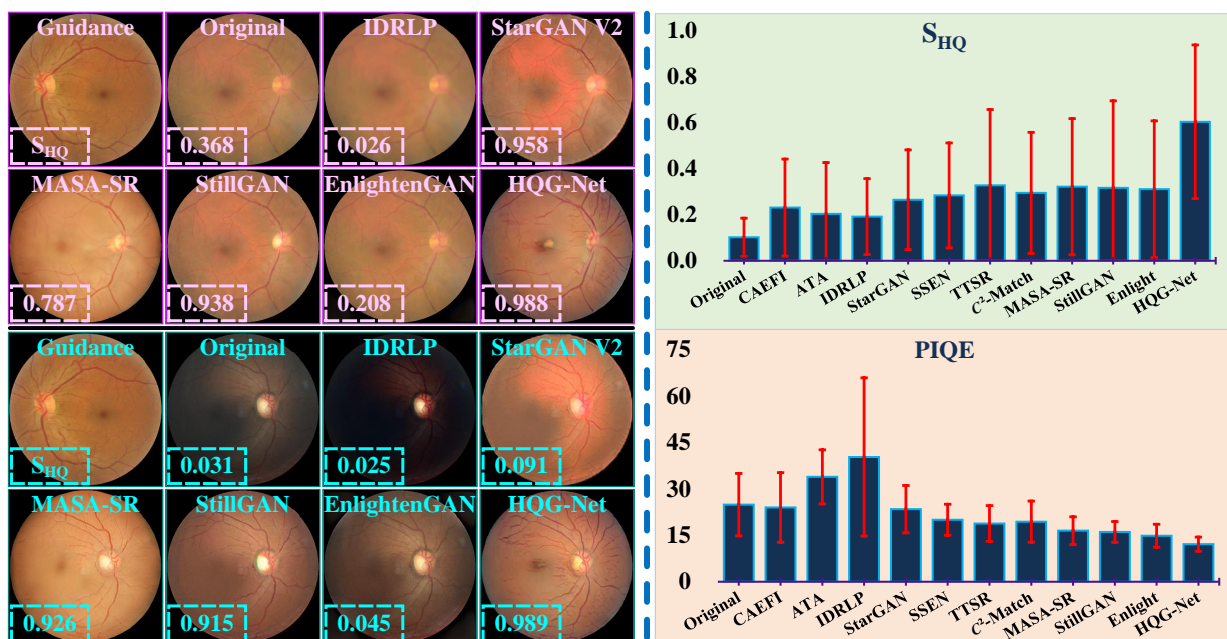


Figure 6: Quantitative and qualitative comparison of the enhanced results on fundus dataset, where StarGAN, C^2 -Match, Enlight are short for StarGAN V2, C^2 -Matching, EnlightenGAN. A larger value in S_{HQ} means better performance, while that is reversed in PIQE. The S_{HQ} of the HQ guidance is 0.986.

EnlightenGAN+, and HQG-Net+, where + means the network is trained with the cooperative training strategy, and the higher metric scores obtained by all the re-trained networks indicate the generalization and effectiveness of the cooperative strategy.

The visualization results are presented in Fig. 5, where we only present partially enhanced results for space limitation. As shown in Fig. 5, CAEFI fails to enhance the LQ image with good visual fidelity. StarGAN V2 utilizes the same guidance image as our method, while the generated images suffer from texture blur and local luminance distortion, which lies in that the style transfer technique has neither an information maintenance framework nor a degradation-specific loss function.

MASA-SR also fails to preserve critical structures and can be influenced by complex degradation due to its ignorance of the characteristics of medical images. StillGAN fails to enhance texture information and highlight the contrast for lacking the direct involvement of real HQ images in the enhancement, as well as the coarse structure loss. Global illumination uniformity is a problem for EnlightenGAN for the excessive attention to local details. In contrast, the enhanced results from HQG-Net enjoy high contrast and enhanced texture details, which is mainly attributed to the explicit HQ information guided HQG-Net and the content-aware loss function. In addition, the results of HQG-Net+ better conform

Table IV: Parameters (M) and FLOPs (G) with the image size of 384×384 (both the LQ input and the HQ guidance).

	StarGAN V2 [23]	SSEN [47]	TTSR [48]	C^2 -Matching [49]	MASA-SR [50]	StillGAN [1]	EnlightenGAN [16]	HQG-Net
Params (M)	78.95	6.52	7.04	9.68	4.38	58.38	56.37	66.42
FLOPs (G)	259.32	285.34	556.41	300.25	258.04	94.73	98.67	87.33

Table V: Ablation studies. SNR is $SNR_{r=3}$. Colon is short for *Colonoscopy*. “w/” and “w/o” denote with and without. “A→B” means substitute A for B. In (b), const is short for constraints. L_1 and L_2 denote $L_{InterVar}$ and $L_{IntraVar}$. (e) is conducted on the combined feature maps rather than the joint vector \mathbf{v}_c for feature matching. (*,*,*) in (g) means whether using the HF components in vertical, horizontal, and diagonal directions, e.g., (1,0,0) indicates using HF components in the vertical direction while discarding those in horizontal and diagonal directions.

(a) Effect of the HQ guidance mechanism.					(b) Consistency of the guidance representation.					(c) Robustness to the HQ guidance.					
Data	Metrics	w/o guidance	Learnable tensor	w/ guidance	Data	Metrics	w/o const	w/ L_1	w/ L_2	w/ L_1+L_2	Data	Metrics	All data	10 images	1 fixed image
CCM	$SNR \uparrow$	18.62	19.83	22.68	CCM	$SNR \uparrow$	22.68	22.67	22.69	22.67	CCM	$SNR \uparrow$	22.56	22.71	22.68
	Dice \uparrow	0.47	0.48	0.54		Dice \uparrow	0.54	0.54	0.54	0.54		Dice \uparrow	0.54	0.53	0.54
Fundus	$S_{HQ} \uparrow$	0.28	0.34	0.60	Fundus	$S_{HQ} \uparrow$	0.60	0.60	0.60	0.60	Fundus	$S_{HQ} \uparrow$	0.61	0.60	0.60
	PIQE \downarrow	19.92	17.64	12.16		PIQE \downarrow	12.16	12.18	12.25	12.23		PIQE \downarrow	11.93	12.70	12.16
Colon	NIQE \downarrow	7.32	7.05	6.61	Colon	NIQE \downarrow	6.61	6.64	6.60	6.65	Colon	NIQE \downarrow	6.63	6.52	6.61
	Dice \uparrow	0.87	0.89	0.91		Dice \uparrow	0.91	0.90	0.90	0.90		Dice \uparrow	0.90	0.91	0.91

(d) Effect of the joint vector \mathbf{v}_z and AdaLIN.							(e) AdaLIN vs. other integration strategies.					
Data	Metrics	w/o multiscale	$\mathbf{v}_z \rightarrow \mathbf{v}_c$	AdaLIN→AdaLIN	AdaLIN→AdaLIN	w/ AdaLIN	Data	Metrics	Concatenate→AdaLIN	Add→AdaLIN	Multiple→AdaLIN	w/ AdaLIN
CCM	$SNR \uparrow$	21.15	20.73	22.12	21.72	22.68	CCM	$SNR \uparrow$	20.04	20.10	19.86	22.19
	Dice \uparrow	0.51	0.51	0.52	0.50	0.54		Dice \uparrow	0.51	0.51	0.50	0.52
Fundus	$S_{HQ} \uparrow$	0.52	0.53	0.56	0.53	0.60	Fundus	$S_{HQ} \uparrow$	0.50	0.49	0.46	0.55
	PIQE \downarrow	16.73	17.97	14.14	13.72	12.16		PIQE \downarrow	16.38	17.06	16.82	12.94
Colon	NIQE \downarrow	7.74	7.82	7.14	6.90	6.61	Colon	NIQE \downarrow	7.28	7.55	7.73	6.92
	Dice \uparrow	0.84	0.85	0.90	0.88	0.91		Dice \uparrow	0.85	0.84	0.84	0.87

(f) Ablation study of the content-aware loss L_{CA} .							(g) Different combinations of high-frequency components in L_{Haar} .								
Data	Metrics	w/o L_{CA}	$L_{Haar} \rightarrow L_{CA}$	$L_{FC} \rightarrow L_{CA}$	$L_s \rightarrow L_{CA}$	w/ L_{CA}	Data	Metrics	(1,0,0)	(0,1,0)	(0,0,1)	(1,1,0)	(1,0,1)	(0,1,1)	(1,1,1)
CCM	$SNR \uparrow$	21.16	21.45	21.29	21.82	22.68	CCM	$SNR \uparrow$	21.54	21.49	22.03	22.14	22.44	22.46	22.68
	Dice \uparrow	0.48	0.53	0.49	0.51	0.54		Dice \uparrow	0.52	0.51	0.52	0.52	0.53	0.53	0.54
Fundus	$S_{HQ} \uparrow$	0.40	0.48	0.54	0.53	0.60	Fundus	$S_{HQ} \uparrow$	0.46	0.47	0.52	0.53	0.57	0.56	0.60
	PIQE \downarrow	16.30	15.40	13.76	14.81	12.16		PIQE \downarrow	15.37	15.42	14.07	13.85	12.94	12.86	12.16
Colon	NIQE \downarrow	8.71	7.25	7.13	7.36	6.61	Colon	NIQE \downarrow	7.86	7.92	7.73	7.46	7.12	6.97	6.61
	Dice \uparrow	0.80	0.87	0.89	0.83	0.91		Dice \uparrow	0.83	0.82	0.83	0.86	0.89	0.90	0.91

to the definitions of HQ images in Fig. 1. Specifically, the LQ CCM data enhanced by HQG-Net+ can better enhance the texture details than those enhanced by HQG-Net, which owes to the segmentation-oriented cooperative training strategy.

Colonoscopy. We train all the learning-based methods with the private *Colonoscopy* dataset and evaluate the enhancement performance with four metrics, i.e., average gradient (AG) [54], entropy (EN) [55], natural image quality evaluator (NIQE) [56], and blind/reference image spatial quality evaluator (BRISQUE) [57]. A higher value in AG or EN means better results, which is reversed in NIQE and BRISQUE. Table III exhibits the qualitative results, and the proposed HQG-Net has the best performance on all the metrics. Besides, we also demonstrate the superiority of the cooperative training strategy in terms of its capacity to improve enhancement performance. Fig. 5 also demonstrates the superiority of HQG-Net in visual comparison, where our enhanced results have excellent visual fidelity for our variation-guided framework and the task-specific loss function. Moreover, in Fig. 5, profiting from the cooperative training strategy, the enhanced results in HQG-Net+ have more uniform illumination than those in HQG-Net.

Fundus. *Fundus* dataset is used for training the compared networks with 640 HQ images and 700 LQ images. High-quality score (S_{HQ}) [1] and perception-based image quality evaluator (PIQE) [58] are used for evaluation, where a higher value in S_{HQ} or a lower score in PIQE means a better outcome. The qualitative and quantitative analyses are presented in Fig. 6. In qualitative analysis, we achieve the best performance in

S_{HQ} and PIQE, where our S_{HQ} is 0.64 and is almost twice as high as the second-best result. Furthermore, the qualitative analysis also demonstrates that the enhanced fundus image has uniform illumination, enhanced texture details, and excellent visual fidelity. Note that the cooperative training strategy is not applicable to this task for the lack of paired labels.

Computational efficiency. We compare the parameters of deep networks and the corresponding FLOPs (at the size of 384×384) on the enhancement task in Table IV. As shown in Table IV, the proposed HQG-Net achieves the lowest FLOPs, which demonstrates the efficiency of our HQG-Net.

B. Ablation Study

Effect of the HQ cue extraction module. As shown in Table Va, when directly removing the HQ cue extraction module or replacing the HQ vector with a learnable tensor, the enhancement performance greatly declines, which verifies the effectiveness of our HQ guidance mechanism.

Consistency of the guidance representation. Furthermore, to verify the consistency of HQG-Net on the HQ cue extraction, we consider regularizing the HQ vector \mathbf{v}_z to exhibit minimal variance when the HQ guidance image is altered. To achieve this, we add two constraints, namely $L_{InterVar}$ and $L_{IntraVar}$, to minimize the variance in either different homogeneous HQ guidance images or the same HQ guidance image with different views, which are formulated as:

$$L_{InterVar} = \|Gr(\mathbf{v}_{z_1}) - Gr(\mathbf{v}_{z_2})\|_F, \quad (19)$$

$$L_{IntraVar} = \|Gr(\mathbf{v}_{z_1}) - Gr(\mathbf{v}_{z_2})\|_F, \quad (20)$$

Table VI: LQ data enhanced by HQG-Net under the guidance of different data, including medical data and natural data. Medical data are from the three used datasets, i.e., *Fundus*, *CCM*, and *Colonoscopy*. Natural data include the hazy data from RESIDE [51], low-light data from SID [52], noisy data from SIDD [53], and the HQ data from their ground-truth images.

(a) CCM data guided by different medical data.							(b) CCM data guided by different natural data.				
Metrics	HQ <i>CCM</i>	HQ <i>Fundus</i>	HQ <i>Colonoscopy</i>	LQ <i>CCM</i>	LQ <i>Fundus</i>	LQ <i>Colonoscopy</i>	Metrics	HQ natural data	Hazy data [51]	Low-light data [52]	Noisy data [53]
$SNR \uparrow$	22.68	21.14	21.08	19.76	19.15	19.33	$SNR \uparrow$	19.07	18.82	18.73	19.11
Dice \uparrow	0.54	0.52	0.51	0.49	0.47	0.48	Dice \uparrow	0.47	0.46	0.47	0.47

(c) Fundus data guided by different medical data.							(d) Fundus data guided by different natural data.				
Metrics	HQ <i>CCM</i>	HQ <i>Fundus</i>	HQ <i>Colonoscopy</i>	LQ <i>CCM</i>	LQ <i>Fundus</i>	LQ <i>Colonoscopy</i>	Metrics	HQ natural data	Hazy data [51]	Low-light data [52]	Noisy data [53]
$SHQ \uparrow$	0.47	0.60	0.49	0.29	0.35	0.29	$SHQ \uparrow$	0.29	0.29	0.28	0.29
PIQE \downarrow	14.75	12.16	13.82	19.84	17.36	18.72	PIQE \downarrow	19.65	19.43	20.07	19.89

(e) Colonoscopy data guided by different medical data.							(f) Colonoscopy data guided by different natural data.				
Metrics	HQ <i>CCM</i>	HQ <i>Fundus</i>	HQ <i>Colonoscopy</i>	LQ <i>CCM</i>	LQ <i>Fundus</i>	LQ <i>Colonoscopy</i>	Metrics	HQ natural data	Hazy data [51]	Low-light data [52]	Noisy data [53]
$NIQE \downarrow$	6.89	6.83	6.61	7.31	7.12	6.96	$NIQE \downarrow$	7.41	7.17	7.40	7.46
Dice \uparrow	0.90	0.90	0.91	0.87	0.88	0.89	Dice \uparrow	0.87	0.88	0.86	0.87

Figure 7: Robustness analysis with the HQ cue extraction module trained with different data, where we simulate various kinds of noise for the HQ guidance image in *CCM* dataset and evaluate the enhancement performance with $SNR_{r=3}$ and Dice.

where \mathbf{v}_{z_1} and \mathbf{v}_{z_2} are the vectors of two randomly selected HQ guidance images \mathbf{z}_1 and \mathbf{z}_2 . \mathbf{v}_{z^1} and \mathbf{v}_{z^2} are the vectors of HQ images \mathbf{z}^1 and \mathbf{z}^2 , where \mathbf{z}^2 is a different view of \mathbf{z}^1 with the random rotation and flip. As presented in Table Vb, the limited increment from the extra constraints, i.e., $L_{InterVar}$ and $L_{IntraVar}$, indicates that HQG-Net has already learned such consistent representation and thereby extract sufficiently stable HQ cues. This mainly attributes to the explicit regularization of our vector-based HQ guidance mechanism and the implicit constraint of the proposed content-aware loss.

Robustness analysis with the HQ cue extraction module trained with different data. To verify the feasibility to pretrain the HQ cue extraction module G with both HQ and LQ data, we conduct a robustness analysis for HQG-Net with G pretrained with different data, i.e., “HQ data only” and “HQ & LQ data”, by simulating different kinds of noise, including Gaussian, Poisson, and Salt & Pepper noises, for the HQ guidance image. As reported in Fig. 7, G trained with “HQ data only” can be inevitably undermined by the fake HQ guidance with perturbations, while G trained with “HQ & LQ data” can better resist the noises and extract more stable HQ cues. Guided by such HQ cues, HQG-Net can better withstand the complex degradation from the LQ inputs and thereby generate HQ enhanced results.

Robustness to the HQ guidance image. We first attest to whether the proposed HQG-Net is robust to the HQ guidance image and mainly consider three conditions, i.e., all HQ data from the corresponding test set (200 HQ images), 10 HQ images, and ours (1 fixed image), to randomly select the HQ image to guide the enhancement in the test phase. As shown in Table Vc, all three conditions yield similar performance, which evidently verifies our robustness to the HQ guidance image and further indicates that HQG-Net can extract general

HQ cues from the HQ guidance images.

Using other types of images for guidance. To verify the advantage of using the HQ images from the same dataset for guiding the enhancement process, we replace the HQ images with other types of images, namely, (1) HQ heterogeneous medical images from another dataset, (2) LQ medical data, (3) natural images. Table VI shows the results. We can see that these alternative choices produce inferior results to using the HQ images from the same dataset as guidance.

However, as shown in Table VI, when being guided by HQ heterogeneous medical data, HQG-Net still generates promising enhanced results that exceed most comparison methods, which lie in the similarities of HQ medical images (see Fig. 1). For example, both HQ colonoscopy and HQ fundus data hold uniform illumination. Besides, HQG-Net introduces vector-based HQ guidance to ensure the extraction of valid HQ cues and employs the variational information normalization module to guide the enhancement with the concise and general variational information from the HQ cues. Therefore, even when the relevance of the HQ guidance image to the LQ image is not very tight, HQG-Net can also extract some valuable HQ cues and apply them to improve the enhancement performance.

Additionally, as depicted in Table VI, even under the guidance of the least relevant and even seriously degraded data, the enhanced performance is gracefully degraded to our Pix2Pix-based version, which demonstrates that introducing the vector-based HQ guidance in a variational manner is a stable and harmless way to improve the enhancement performance.

To sum up, the superiority of the enhanced results under the highly relevant HQ guidance, i.e., the HQ homogeneous images, and the robustness of them under the least relevant and seriously degraded guidance, i.e., the LQ natural images, validate that *our guidance-based framework is a meaningful*

Table VII: Segmentation results on CCM and Colonoscopy datasets, where the best and the second-best are marked in red and blue. In *CCM* dataset, the cooperative training strategy improves the performance by 6.3% (HQG-Net), 2.9% (EnlightenGAN), 3.8% (StillGAN), 2.8% (MASA-SR), and 14.9% (StarGAN V2). In *Colonoscopy* dataset, such a training strategy increases that by 1.3% (HQG-Net), 2.0% (EnlightenGAN), 1.1% (StillGAN), 2.4% (MASA-SR), and 28.2% (StarGAN V2).

Methods	CCM					Colonoscopy				
	AUC↑	ACC↑	SEN↑	Dice↑	G_Mean↑	AUC↑	ACC↑	SEN↑	Dice↑	G_Mean↑
Original	0.877	0.982	0.492	0.387	0.674	0.965	0.978	0.871	0.885	0.914
CAEFI [9]	0.919	0.951	0.815	0.352	0.886	0.959	0.974	0.841	0.856	0.895
ATA [10]	0.936	0.976	0.815	0.483	0.869	0.961	0.972	0.842	0.855	0.891
IDRLP [11]	0.931	0.975	0.765	0.477	0.866	0.764	0.914	0.407	0.407	0.493
StarGAN V2 [23]	0.851	0.948	0.642	0.244	0.775	0.792	0.926	0.411	0.459	0.514
SSEN [47]	0.922	0.973	0.818	0.445	0.857	0.967	0.972	0.854	0.877	0.910
TTSR [48]	0.917	0.968	0.814	0.468	0.861	0.965	0.964	0.847	0.894	0.922
C^2 -Matching [49]	0.915	0.977	0.821	0.472	0.854	0.973	0.968	0.851	0.872	0.906
MASA-SR [50]	0.928	0.975	0.825	0.497	0.874	0.969	0.975	0.862	0.891	0.918
StillGAN [1]	0.942	0.973	0.831	0.488	0.879	0.976	0.979	0.856	0.901	0.931
EnlightenGAN [16]	0.929	0.969	0.771	0.457	0.887	0.965	0.978	0.887	0.879	0.907
HQG-Net	0.951	0.984	0.837	0.536	0.893	0.978	0.981	0.891	0.906	0.930
StarGAN V2+	0.871	0.968	0.685	0.390	0.801	0.836	0.964	0.537	0.663	0.802
MASA-SR+	0.934	0.976	0.840	0.542	0.883	0.970	0.980	0.888	0.913	0.930
StillGAN+	0.950	0.971	0.851	0.557	0.886	0.976	0.981	0.878	0.916	0.941
EnlightenGAN+	0.934	0.972	0.788	0.502	0.891	0.971	0.982	0.896	0.906	0.922
HQG-Net+	0.963	0.991	0.872	0.663	0.907	0.982	0.986	0.910	0.924	0.943

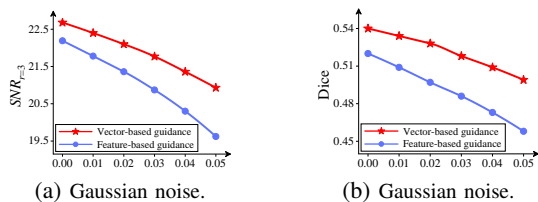


Figure 8: Robustness analysis with vector-based guidance (ours) and feature-based guidance, where we simulate Gaussian noise for the HQ guidance image in *CCM* dataset.

exploration for the UMIE task and can draw the attention of the community to handle the UMIE task with the explicit assistance of reference images. Besides, considering that it is very easy for a hospital to obtain an HQ image that is highly correlated with the LQ image, e.g., LQ and HQ data acquired by the same instrument with the same set of parameters for the same organs, our HQG-Net has a high clinical utility.

Effect of the vector-based guidance. We further validate the efficacy of the vector-based guidance with the joint vector \mathbf{v}_c . In Fig. 8, HQG-Net with vector-based guidance can better enhance LQ images and moderate the slight perturbations from the HQ guidance, which verifies that the vector-based guidance helps to extract valid HQ cues. Besides, as exhibited in Table Vd, guided by the joint vector \mathbf{v}_z that combines the HQ vector \mathbf{v}_z and structure vector \mathbf{v}_c , HQG-Net is capable of preserving critical structural information and achieving superior enhancement performance.

Effect of the variational information normalization module. We verify the effect of the variational information normalization module by ablating AdaLIN (Table Vd) and comparing AdaLIN with other integration strategies at the feature level (Table Ve). In Table Vd, by canceling the multiscale strategy and ablating AdaLIN, we validate the effect of the multiscale AdaLIN operator. Besides, when substituting AdaLIN for other integration strategies, namely feature-level concatenate, add, or multiple, we directly use the combined feature maps rather than the joint vector \mathbf{v}_c for feature matching. For fair-

ness, we also provide the results of AdaLIN with the combined features. Table Ve validates the superiority of AdaLIN over other information integration strategies, which attributes to the concise and general variational information from AdaLIN.

Effect of the content-aware loss. We further ablate the content-aware loss L_{CA} (Table Vf) and evaluate the optimal combination in L_{Haar} (Table Vg). In Table Vf, we compare several combinations of loss functions, where L_s is the structure loss in StillGAN [1]. Table Vf attests to the superiority of our content-aware loss. Besides, as shown in Table Vg, we try the different combinations of high-frequency components in L_{Haar} and find that combining all the high-frequency subbands results in optimal enhancement performance.

C. Downstream Tasks

Medical image segmentation task. Thanks to the paired segmented label for the *CCM* and *Colonoscopy* datasets, we further test the segmentation results with the corresponding segmentors, i.e., CS-Net [7] and PNS-Net [6] with their pre-trained models. Five commonly used metrics are applied for assessment, i.e., area under the ROC curve (AUC), accuracy (ACC), sensitivity (SEN), Dice coefficient (Dice), and G-mean score (G-Mean), where a higher value indicates a better performance. As shown in Table VII, the proposed HQG-Net achieves nine best values and one second-best value in the ten scores, demonstrating that the image enhanced by our method can best facilitate the downstream segmentation task. As shown in Fig. 9, the segmented results of HQG-Net are more accurate and continuous, which further verifies the superiority of HQG-Net for the highlight of the geometric structure, whether the foreground is filamentous or blocky. Moreover, in Table VII, compared with networks optimized solely with the enhancement loss, the corresponding network optimized by our cooperative training strategy achieves better performance, indicating the potential of the cooperative training strategy to generate enhancement results that are segmentation-friendly.

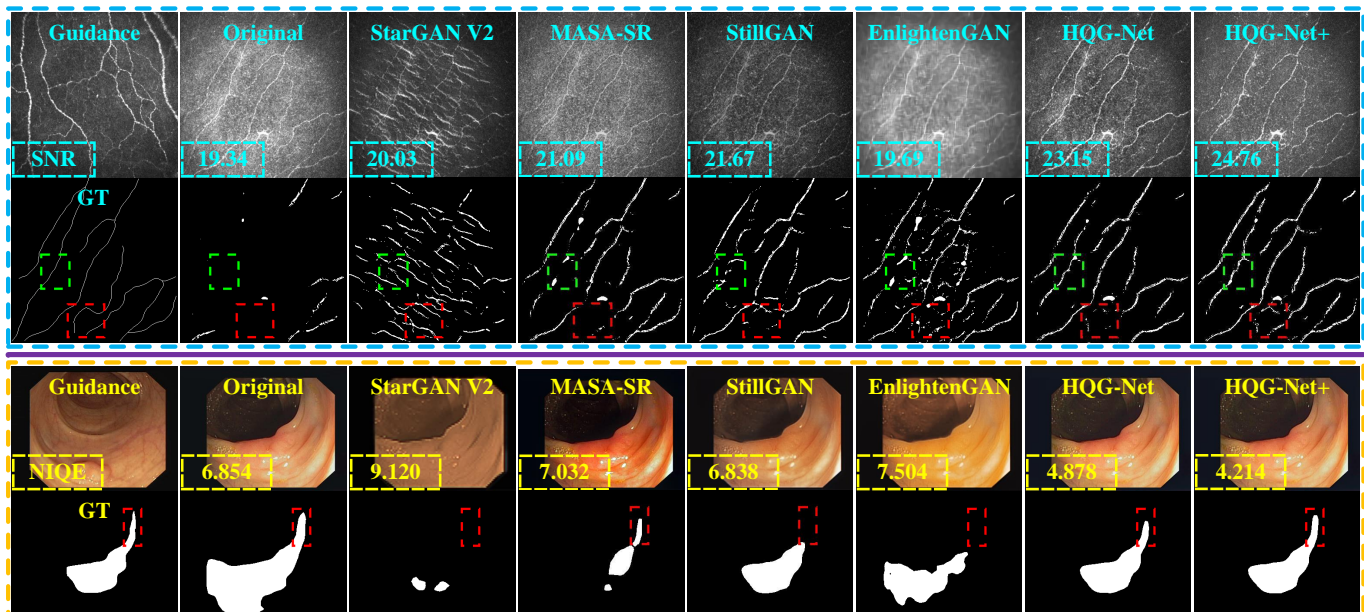


Figure 9: Visual comparison on CCM and Colonoscopy, where guidance images and segmentation results are also presented.

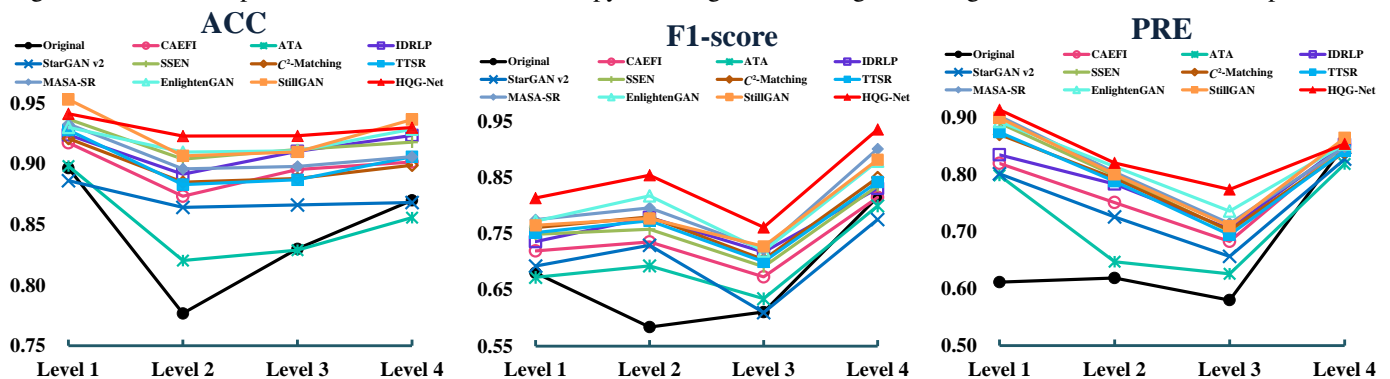


Figure 10: Nerve fiber tortuosity classification under different methods on CORN-3 dataset with ACC, F1-score, and PRE.

Table VIII: Generalization of our cooperative training strategy, where Enlight is short for EnlightenGAN and “+” denotes optimizing the method under the cooperative training strategy. Increases are marked in red.

(a) Accuracy of nerve fiber tortuosity classification.

Tortuosity	HQG-Net	HQG-Net+	StillGAN	StillGAN+	Enlight	Enlight+
Level 1	0.941	0.972 (+0.031)	0.953	0.978 (+0.025)	0.930	0.961 (+0.031)
Level 2	0.923	0.931 (+0.008)	0.906	0.922 (+0.016)	0.909	0.920 (+0.011)
Level 3	0.923	0.947 (+0.024)	0.910	0.931 (+0.021)	0.911	0.926 (+0.015)
Level 4	0.930	0.952 (+0.022)	0.936	0.949 (+0.013)	0.929	0.946 (+0.017)

(b) F1-score of nerve fiber tortuosity classification.

Tortuosity	HQG-Net	HQG-Net+	StillGAN	StillGAN+	Enlight	Enlight+
Level 1	0.813	0.835 (+0.022)	0.765	0.796 (+0.031)	0.772	0.785 (+0.013)
Level 2	0.854	0.876 (+0.022)	0.777	0.813 (+0.036)	0.817	0.858 (+0.041)
Level 3	0.761	0.811 (+0.050)	0.727	0.771 (+0.044)	0.719	0.764 (+0.045)
Level 4	0.935	0.942 (+0.007)	0.882	0.906 (+0.024)	0.879	0.895 (+0.016)

Nerve fiber tortuosity classification task. Previous studies indicate that the tortuosity level grading in CCM is highly relevant to some diseases [59], [60], e.g., diabetic neuropathy and hypertensive retinopathy. Hence, we conduct an experiment on nerve fiber tortuosity with a SOTA classifier, Deepgrading [44], to explore how the enhancement task contributes to disease-related classifications on *CORN-3* dataset [1], which contains about 300 images that are divided into four levels according to the tortuosity level. Three metrics are used to estimate the performance, i.e., ACC, F1-score, and precision (PRE), where a higher value means better performance. In Fig. 10, the proposed HQG-Net achieves ten best and two second-best values among the twelve metrics, which shows that the proposed HQG-Net can improve the identification rate of nerve fiber tortuosity and further demonstrate the clinical

value of HQG-Net. In addition, as shown in Table VIII, the cooperative training strategy improves the accuracy of nerve fiber tortuosity classification by 2.3% (HQG-Net), 2.0% (StillGAN), 2.1% (EnlightenGAN), and increases the F1-score of that by 3.2% (HQG-Net), 4.4% (StillGAN), 3.7% (EnlightenGAN). These increments provide strong evidence of the superiority of the cooperative training strategy.

D. Clinical Decision-Making

Medical image reclassification task. In the image reclassification task, we invite two collaborative clinicians, who have participated in the production of our private datasets, to reclassify the LQ images (60 in *CCM* and 70 in *Colonoscopy*) and the HQ images (200 in *CCM* and 200 in *Colonoscopy*) enhanced by HQG-Net and HQG-Net+, where we randomly

Table IX: Medical image reclassification of HQG-Net and HQG-Net+ on the enhanced LQ data and re-enhanced HQ data in *CCM* and *Colonoscopy* datasets. The table shows the count of images that can be classified as HQ data from the experts’ view.

(a) Image reclassification on the enhanced LQ data.							(b) Image reclassification on the re-enhanced HQ data.						
Experts	<i>CCM</i> (60 images)			<i>Colonoscopy</i> (70 images)			Experts	<i>CCM</i> (200 images)			<i>Colonoscopy</i> (200 images)		
	Original	HQG-Net	HQG-Net+	Original	HQG-Net	HQG-Net+		Original	HQG-Net	HQG-Net+	Original	HQG-Net	HQG-Net+
Clinician 1	0	43	47 (+9.3%)	0	55	59 (+7.3%)	Clinician 1	200	200	200	200	200	200
Clinician 2	0	46	51 (+10.9%)	0	58	61 (+5.2%)	Clinician 2	200	200	200	200	200	200

Table X: Disease diagnosis of original LQ data and those enhanced by our HQG-Net on the newly collected *DiaRet* dataset.

(a) ACC of disease diagnosis.			(b) SEN of disease diagnosis.			(c) F1-score of disease diagnosis.			(d) PRE of disease diagnosis.		
Experts	Original	HQG-Net	Experts	Original	HQG-Net	Experts	Original	HQG-Net	Experts	Original	HQG-Net
Clinician 1	0.745	0.825 (+10.7%)	Clinician 1	0.810	0.840 (+3.7%)	Clinician 1	0.755	0.820 (+8.6%)	Clinician 1	0.727	0.815 (+12.1%)
Clinician 2	0.735	0.830 (+12.9%)	Clinician 2	0.820	0.845 (+3.0%)	Clinician 2	0.761	0.836 (+9.7%)	Clinician 2	0.719	0.844 (+17.4%)

select homogeneous HQ guidance in the enhancement. To avoid bias from the experts, we leave out that these images have already been enhanced. As shown in Table IXa, both HQG-Net and HQG-Net+ achieve promising performance in this reclassification task, which verifies that HQG-Net and HQG-Net+ have been successful in improving the quality of most LQ images from a clinical perspective. While in Table IXb, none of the enhanced HQ images are identified as the LQ ones, thereby confirming that both HQG-Net and HQG-Net+ do not weaken the quality of the enhanced images.

Disease diagnosis task. In the disease diagnosis task, we create a new dataset, *DiaRet*, comprised of 300 LQ fundus images, obtained from 150 healthy eyes and 150 eyes affected by diabetic retinopathy. These images were selected from the “usable” grade of the Eye-Quality [61] with their labels, i.e., with or without diabetic retinopathy. We invite two ophthalmologists to diagnose diabetic retinopathy from the given images, i.e., the original data and the data enhanced by our HQG-Net. To minimize subjective factors, the ophthalmologists are invited to perform the diagnostic task based on the original data first and to review the enhanced images three days later. The diagnostic results from the two ophthalmologists are presented in Table X, where HQG-Net improves the diagnosis results by 11.8% (ACC), 3.4% (SEN), 9.2% (F1-score), and 14.8% (PRE). Such results firmly demonstrate that HQG-Net is a promising method for facilitating clinical decision-making.

V. CONCLUSION

In this paper, we propose a GAN-based network for unpaired medical image enhancement with the explicit guidance of unpaired HQ images (HQG-Net), which is the first work to model the medical image enhancement task under the joint distribution between both the LQ and HQ domains. The joint distribution-based framework implicitly contains more comprehensive and unbiased information than those methods, which only rely on the LQ domain. Therefore, HQG-Net can generate enhanced images with better visual fidelity. For high image contrast and enhanced textural details, the content-aware loss function is proposed with both wavelet-based pixel-level and feature-level consistency constraints. We further propose a bi-level formulation to jointly optimize the UMIE framework with the downstream tasks. Compared with the state-of-the-art techniques, the proposed HQG-Net achieves the best performance in the three distinct modalities both in

the medical enhancement problem and the subsequent applicability validation tasks. *Fundus* and *Colonoscopy* datasets with enhanced quality labels will be released to the public with the source code in the future for community research.

VI. ACKNOWLEDGMENT

The authors would like to express their sincere appreciation to the anonymous reviewers for their insightful comments, which greatly improved the quality of this paper.

REFERENCES

- [1] Y. Ma, J. Liu, Y. Liu, H. Fu, Y. Hu, J. Cheng, H. Qi, Y. Wu, J. Zhang, and Y. Zhao, “Structure and illumination constrained gan for medical image enhancement,” *IEEE Trans. Med. Imaging*, vol. 40, no. 12, pp. 3955–3967, 2021. 1, 2, 3, 4, 5, 7, 8, 9, 11, 12
- [2] M. Ikuta and J. Zhang, “A deep convolutional gated recurrent unit for ct image reconstruction,” *IEEE Trans. Neural Networks Learn. Syst.*, 2022. 1
- [3] G. Xu, C. He, H. Wang, H. Zhu, and W. Ding, “Dm-fusion: Deep model-driven network for heterogeneous image fusion,” *IEEE Transactions on Neural Networks and Learning Systems*, 2023. 1
- [4] Y. Shen, X. Jia, and M. Q.-H. Meng, “Hrenet: A hard region enhancement network for polyp segmentation,” in *MICCAI*. Springer, 2021, pp. 559–568. 1
- [5] Y. Zhou, H. Yu, and H. Shi, “Study group learning: Improving retinal vessel segmentation trained with noisy labels,” in *MICCAI*. Springer, 2021, pp. 57–67. 1
- [6] G.-P. Ji, Y.-C. Chou, D.-P. Fan, G. Chen, H. Fu, D. Jha, and L. Shao, “Progressively normalized self-attention network for video polyp segmentation,” in *MICCAI*. Springer, 2021, pp. 142–152. 1, 6, 11
- [7] L. Mou, Y. Zhao, L. Chen, J. Cheng, Z. Gu, H. Hao, H. Qi, Y. Zheng, A. Frangi, and J. Liu, “Cs-net: channel and spatial attention network for curvilinear structure segmentation,” in *MICCAI*. Springer, 2019, pp. 721–730. 1, 6, 11
- [8] Y. He, R. Ge, X. Qi, Y. Chen, J. Wu, J.-L. Coatrieux, G. Yang, and S. Li, “Learning better registration to learn better few-shot medical image segmentation: Authenticity, diversity, and robustness,” *IEEE Trans. Neural Networks Learn. Syst.*, 2022. 1
- [9] H. Jeelani, H. Liang, S. T. Acton, and D. S. Weller, “Content-aware enhancement of images with filamentous structures,” *IEEE Trans. Image Process.*, vol. 28, no. 7, pp. 3451–3461, 2019. 1, 3, 7, 8, 11
- [10] Y. Zhao, J. Zhang, E. Pereira, Y. Zheng, P. Su, J. Xie, Y. Zhao, Y. Shi, H. Qi, J. Liu *et al.*, “Automated tortuosity analysis of nerve fibers in corneal confocal microscopy,” *IEEE Trans. Med. Imaging*, vol. 39, no. 9, pp. 2725–2737, 2020. 1, 3, 5, 7, 8, 11
- [11] M. Ju, C. Ding, C. A. Guo, W. Ren, and D. Tao, “Idrlp: image dehazing using region line prior,” *IEEE Trans. Image Process.*, vol. 30, pp. 9043–9057, 2021. 1, 3, 7, 8, 11
- [12] P. Isola, J.-Y. Zhu, T. Zhou, and A. A. Efros, “Image-to-image translation with conditional adversarial networks,” in *CVPR*, 2017, pp. 1125–1134. 1, 3
- [13] C. He, K. Li, Y. Zhang, L. Tang, Y. Zhang, Z. Guo, and X. Li, “Camouflaged object detection with feature decomposition and edge reconstruction,” in *Proceedings of the IEEE/CVF Conference on Computer Vision and Pattern Recognition*, 2023, pp. 22046–22055. 1, 5

- [14] C. He, K. Li, Y. Zhang, G. Xu, L. Tang, Y. Zhang, Z. Guo, and X. Li, "Weakly-supervised concealed object segmentation with sam-based pseudo labeling and multi-scale feature grouping," *arXiv preprint arXiv:2305.11003*, 2023. **1**
- [15] L. Xu, H. Wu, C. He, J. Wang, C. Zhang, F. Nie, and L. Chen, "Multi-modal sequence learning for alzheimer's disease progression prediction with incomplete variable-length longitudinal data," *Medical Image Analysis*, vol. 82, p. 102643, 2022. **1**
- [16] Y. Jiang, X. Gong, D. Liu, Y. Cheng, C. Fang, X. Shen, J. Yang, P. Zhou, and Z. Wang, "Enlightengan: Deep light enhancement without paired supervision," *IEEE Trans. Image Process.*, vol. 30, pp. 2340–2349, 2021. **1, 3, 7, 8, 9, 11**
- [17] J.-Y. Zhu, T. Park, P. Isola, and A. A. Efros, "Unpaired image-to-image translation using cycle-consistent adversarial networks," in *ICCV*, 2017, pp. 2223–2232. **2, 3**
- [18] Z. Yue, Q. Zhao, L. Zhang, and D. Meng, "Dual adversarial network: Toward real-world noise removal and noise generation," in *ECCV*. Springer, 2020, pp. 41–58. **2**
- [19] L. Xu, R. Wang, F. Nie, and X. Li, "Efficient top-k feature selection using coordinate descent method," in *Proceedings of the AAAI Conference on Artificial Intelligence*, vol. 37, no. 9, Jun. 2023, pp. 10594–10601. **2**
- [20] J. Xie, F. Long, J. Lv, Q. Wang, and P. Li, "Joint distribution matters: Deep brownian distance covariance for few-shot classification," in *CVPR*, 2022, pp. 7972–7981. **2**
- [21] F. Yu, L. Cui, H. Chen, Y. Cao, N. Liu, W. Huang, Y. Xu, and H. Lu, "Healthnet: A health progression network via heterogeneous medical information fusion," *IEEE Trans. Neural Networks Learn. Syst.*, 2022. **2**
- [22] F. E. Fernandes and G. G. Yen, "Automatic searching and pruning of deep neural networks for medical imaging diagnostic," *IEEE Trans. Neural Networks Learn. Syst.*, vol. 32, no. 12, pp. 5664–5674, 2020. **2**
- [23] Y. Choi, Y. Uh, J. Yoo, and J.-W. Ha, "Stargan v2: Diverse image synthesis for multiple domains," in *CVPR*, 2020, pp. 8188–8197. **3, 4, 7, 8, 9, 11**
- [24] M. Abdullah-Al-Wadud, M. H. Kabir, M. A. A. Dewan, and O. Chae, "A dynamic histogram equalization for image contrast enhancement," *IEEE Trans. Consumer Electron.*, vol. 53, no. 2, pp. 593–600, 2007. **3**
- [25] M. Foracchia, E. Grisan, and A. Ruggeri, "Luminosity and contrast normalization in retinal images," *Med. Image Anal.*, vol. 9, no. 3, pp. 179–190, 2005. **3**
- [26] A. W. Setiawan, T. R. Mengko, O. S. Santoso, and A. B. Suksmono, "Color retinal image enhancement using clahe," in *ICISS*. IEEE, 2013, pp. 1–3. **3**
- [27] H. Liao, W.-A. Lin, S. K. Zhou, and J. Luo, "Adn: artifact disentanglement network for unsupervised metal artifact reduction," *IEEE Trans. Med. Imaging*, vol. 39, no. 3, pp. 634–643, 2019. **3**
- [28] Y. Men, Y. Yao, M. Cui, Z. Lian, X. Xie, and X.-S. Hua, "Unpaired cartoon image synthesis via gated cycle mapping," in *CVPR*, 2022, pp. 3501–3510. **4**
- [29] H. Zheng, M. Ji, H. Wang, Y. Liu, and L. Fang, "Crossnet: An end-to-end reference-based super resolution network using cross-scale warping," in *ECCV*, 2018, pp. 88–104. **4**
- [30] Z. Zhang, Z. Wang, Z. Lin, and H. Qi, "Image super-resolution by neural texture transfer," in *CVPR*, 2019, pp. 7982–7991. **4**
- [31] T. Karras, S. Laine, and T. Aila, "A style-based generator architecture for generative adversarial networks," in *CVPR*, 2019, pp. 4401–4410. **4**
- [32] Z. Shen, H. Fu, J. Shen, and L. Shao, "Modeling and enhancing low-quality retinal fundus images," *IEEE Trans. Med. Imaging*, vol. 40, no. 3, pp. 996–1006, 2020. **4**
- [33] J. Liu, X. Fan, Z. Huang, G. Wu, R. Liu, W. Zhong, and Z. Luo, "Target-aware dual adversarial learning and a multi-scenario multi-modality benchmark to fuse infrared and visible for object detection," in *CVPR*, 2022, pp. 5802–5811. **4**
- [34] X. Huang and S. Belongie, "Arbitrary style transfer in real-time with adaptive instance normalization," in *ICCV*, 2017, pp. 1501–1510. **5**
- [35] B. Zhang, S. Gu, B. Zhang, J. Bao, D. Chen, F. Wen, Y. Wang, and B. Guo, "Styleswin: Transformer-based gan for high-resolution image generation," in *CVPR*, 2022, pp. 11304–11314. **5**
- [36] C. Li and M. Wand, "Precomputed real-time texture synthesis with markovian generative adversarial networks," in *ECCV*. Springer, 2016, pp. 702–716. **5**
- [37] L. Deng, C. He, G. Xu, H. Zhu, and H. Wang, "Pcgan: A noise robust conditional generative adversarial network for one shot learning," *IEEE Transactions on Intelligent Transportation Systems*, vol. 23, no. 12, pp. 25249–25258, 2022. **5**
- [38] J. Ma, C. Chen, C. Li, and J. Huang, "Infrared and visible image fusion via gradient transfer and total variation minimization," *Inf. Fusion*, vol. 31, pp. 100–109, 2016. **5**
- [39] J. Yoo, Y. Uh, S. Chun, B. Kang, and J.-W. Ha, "Photorealistic style transfer via wavelet transforms," in *ICCV*, 2019, pp. 9036–9045. **5**
- [40] A. Kacem, M. Daoudi, B. B. Amor, S. Berretti, and J. C. Alvarez-Paiva, "A novel geometric framework on gram matrix trajectories for human behavior understanding," *IEEE Trans. Pattern Anal. Mach. Intell.*, vol. 42, no. 1, pp. 1–14, 2018. **5**
- [41] M. Ju, C. He, J. Liu, B. Kang, J. Su, and D. Zhang, "Ivf-net: An infrared and visible data fusion deep network for traffic object enhancement in intelligent transportation systems," *IEEE Transactions on Intelligent Transportation Systems*, vol. 24, no. 1, pp. 1220–1234, 2022. **6**
- [42] R. Liu, L. Ma, X. Yuan, S. Zeng, and J. Zhang, "Task-oriented convex bilevel optimization with latent feasibility," *IEEE Trans. Image Process.*, vol. 31, pp. 1190–1203, 2022. **6**
- [43] P. Ochs, R. Ranftl, T. Brox, and T. Pock, "Bilevel optimization with nonsmooth lower level problems," in *SSVM*. Springer, 2015, pp. 654–665. **6**
- [44] L. Mou, H. Qi, Y. Liu, Y. Zheng, P. Matthew, P. Su, J. Liu, J. Zhang, and Y. Zhao, "Deepgrading: Deep learning grading of corneal nerve tortuosity," *IEEE Trans. Med. Imaging*, 2022. **6, 12**
- [45] Y. Yan, M. Tan, Y. Xu, J. Cao, M. Ng, H. Min, and Q. Wu, "Oversampling for imbalanced data via optimal transport," in *AAAI*, vol. 33, no. 01, 2019, pp. 5605–5612. **7**
- [46] D. Vázquez, J. Bernal, F. J. Sánchez, G. Fernández-Esparrach, A. M. López, A. Romero, M. Drozdal, and A. Courville, "A benchmark for endoluminal scene segmentation of colonoscopy images," *J. Healthc. Eng.*, vol. 2017, 2017. **7**
- [47] G. Shim, J. Park, and I. S. Kweon, "Robust reference-based super-resolution with similarity-aware deformable convolution," in *CVPR*, 2020, pp. 8425–8434. **7, 8, 9, 11**
- [48] F. Yang, H. Yang, J. Fu, H. Lu, and B. Guo, "Learning texture transformer network for image super-resolution," in *CVPR*, 2020, pp. 5791–5800. **7, 8, 9, 11**
- [49] Y. Jiang, K. C. Chan, X. Wang, C. C. Loy, and Z. Liu, "Robust reference-based super-resolution via c2-matching," in *CVPR*, 2021, pp. 2103–2112. **7, 8, 9, 11**
- [50] L. Lu, W. Li, X. Tao, J. Lu, and J. Jia, "Masa-sr: Matching acceleration and spatial adaptation for reference-based image super-resolution," in *CVPR*, 2021, pp. 6368–6377. **7, 8, 9, 11**
- [51] B. Li, W. Ren, D. Fu, D. Tao, D. Feng, W. Zeng, and Z. Wang, "Benchmarking single-image dehazing and beyond," *IEEE Trans. Image Process.*, vol. 28, no. 1, pp. 492–505, 2018. **10**
- [52] C. Chen, Q. Chen, J. Xu, and V. Koltun, "Learning to see in the dark," in *CVPR*, 2018, pp. 3291–3300. **10**
- [53] A. Abdelhamed, S. Lin, and M. S. Brown, "A high-quality denoising dataset for smartphone cameras," in *CVPR*, 2018, pp. 1692–1700. **10**
- [54] J. Wu, H. Huang, Y. Qiu, H. Wu, J. Tian, and J. Liu, "Remote sensing image fusion based on average gradient of wavelet transform," in *ICMA*, vol. 4. IEEE, 2005, pp. 1817–1821. **9**
- [55] D. Haussler and M. Opper, "Mutual information, metric entropy and cumulative relative entropy risk," *Ann. Stat.*, vol. 25, no. 6, pp. 2451–2492, 1997. **9**
- [56] A. Mittal, R. Soundararajan, and A. C. Bovik, "Making a "completely blind" image quality analyzer," *IEEE Signal Process. Lett.*, vol. 20, no. 3, pp. 209–212, 2012. **9**
- [57] A. Mittal, A. K. Moorthy, and A. C. Bovik, "No-reference image quality assessment in the spatial domain," *IEEE Trans. Image Process.*, vol. 21, no. 12, pp. 4695–4708, 2012. **9**
- [58] L. Zhang, L. Zhang, and A. C. Bovik, "A feature-enriched completely blind image quality evaluator," *IEEE Trans. Image Process.*, vol. 24, no. 8, pp. 2579–2591, 2015. **9**
- [59] K. Zhou, J. Li, Y. Xiao, J. Yang, J. Cheng, W. Liu, W. Luo, J. Liu, and S. Gao, "Memorizing structure-texture correspondence for image anomaly detection," *IEEE Trans. Neural Networks Learn. Syst.*, 2021. **12**
- [60] C. He, X. Wang, L. Deng, and G. Xu, "Image threshold segmentation based on gile histogram," in *2019 International Conference on Internet of Things (iThings) and IEEE Green Computing and Communications (GreenCom) and IEEE Cyber, Physical and Social Computing (CPSCom) and IEEE Smart Data (SmartData)*. IEEE, 2019, pp. 410–415. **12**
- [61] H. Fu, B. Wang, J. Shen, S. Cui, Y. Xu, J. Liu, and L. Shao, "Evaluation of retinal image quality assessment networks in different color-spaces," in *MICCAI*. Springer, 2019, pp. 48–56. **13**